RESEARCH ARTICLE

Scalable Fabrication of MXene-PVDF Nanocomposite Triboelectric Fibers via Thermal Drawing

Md Mehdi Hasan, Md Sazid Bin Sadeque, Ilgın Albasar, Hilal Pecenek, Fatma Kilic Dokan, M. Serdar Onses, and Mustafa Ordu*

In the data-driven world, textile is a valuable resource for improving the quality of life through continuous monitoring of daily activities and physiological signals of humans. Triboelectric nanogenerators (TENG) are an attractive option for self-powered sensor development by coupling energy harvesting and sensing ability. In this study, to the best of the knowledge, scalable fabrication of $Ti_3C_2T_x$ MXene-embedded polyvinylidene fluoride (PVDF) nanocomposite fiber using a thermal drawing process is presented for the first time. The output open circuit voltage and short circuit current show 53% and 58% improvement, respectively, compared to pristine PVDF fiber. The synergistic interaction between the surface termination groups of MXene and polar PVDF polymer enhances the performance of the fiber. The flexibility of the fiber enables the weaving of fabric TENG devices for large-area applications. The fabric TENG (3×2 cm^2) demonstrates a power density of 40.8 mW m^{-2} at the matching load of 8 MΩ by maintaining a stable performance over 12 000 cycles. Moreover, the fabric TENG has shown the capability of energy harvesting by operating a digital clock and a calculator. A distributed self-powered sensor for human activities and walking pattern monitoring are demonstrated with the fabric.

M. M. Hasan, M. S. B. Sadeque, I. Albasar, M. S. Onses, M. Ordu
UNAM – Institute of Materials Science and Nanotechnology
Bilkent University
Ankara 06800, Turkey
E-mail: ordu@unam.bilkent.edu.tr

I. Albasar
Department of Materials Science and Nanotechnology Engineering
TOBB University of Economics and Technology
Ankara 06560, Turkey

H. Pecenek, M. S. Onses
ERNAM – Erciyes University Nanotechnology Application and Research Center
Kayseri 38039, Turkey

F. K. Dokan
Department of Chemistry and Chemical Processing Technologies
Mustafa Çıkrıkçıoglu Vocational School
Kayseri University
Kayseri 38280, Turkey

M. S. Onses
Department of Materials Science and Engineering
Faculty of Engineering
Erciyes University
Kayseri 38039, Turkey

1. Introduction

The nanotechnology revolution has enabled the fabrication of various functional devices for flexible and wearable electronics applications. Wearable devices have the potential to improve the way of life through continuous monitoring of vital signals of the human body.[1–3] Textiles being the most ubiquitous element of human life get exposed to an immense amount of physiological data.[4] Several forms of textile-based sensors, that is, capacitive,[5] piezoresistive,[6] optical,[7] and nanogenerator-based[8] sensors have been reported to collect data for continuous monitoring. Nanogenerator-based sensors work on piezoelectric (PENG),[9] triboelectric (TENG),[10] thermoelectric (TEG),[11] and electromagnetic (EMG)[12] principles, and have the unique advantage of energy harvesting from mechanical motion. The capability of scavenging energy of nanogenerators provides a competitive edge over other devices for the development of next-generation sensors due to the potential for the development of self-powered sensors. The self-powered sensor module may emerge as the missing piece for developing true flexible electronics by eliminating rigid and bulky batteries that require frequent replacement and recharging. TENG has emerged as an attractive option due to the possibility of harvesting mechanical energy from the friction of, theoretically, any material. TENG functions through contact electrification and the electrostatic induction principle.[13] TENG harvests energy by charge generation during the contact-separation movement of two material surfaces with different electron affinities. However, the efficient energy harvesting capability of TENG is fundamental to meeting the energy demand for real-world applications, and the appropriate choice of materials is one of the dominating factors for achieving superior performance.

A wide range of polar polymeric materials has been proposed for the development of flexible TENGs.[14] Among these materials, especially ferroelectric fluoropolymers, that is, polyvinylidene fluoride (PVDF) based polymers, stand out owing to excellent flexibility, electronegativity, and spontaneous yet stable and tunable polarization.[15,16] Several strategies have been proposed to improve charge generation and charge storage capacity to improve TENG performance including ion

injection,[17] surface functionalization,[18] spontaneous polarization,[19] dielectric constant increment,[20] and charge trapping interlayer inclusion.[21] As the dielectric property is directly related to surface charge density, optimization of the dielectric constant is an attractive option for performance enhancement due to the direct relation with surface charge density and the availability of well-established methodologies for dielectric tuning via micro and nanomaterial incorporation.[22,23]

Different nanomaterials ranging from 0D to 2D have been studied for the enhancement of TENG output.[24–26] 2D nanomaterials, for example, graphene oxide (GO), transition metal dichalcogenides (TMDs), MXenes, black phosphorus (BP), layered metal-organic frameworks (MOFs), layered covalent-organic frameworks (COFs), hexagonal boron nitride (h-BN), and layered metals, possess superior physical, chemical, mechanical, electrical, and optical properties along with high surface area. Transition metal carbides/nitrides, or more commonly MXenes, are a contemporary class of 2D nanomaterials that have gained immense interest in the field of flexible electronics owing to excellent conductivity, mechanical properties, chemical stability, hydrophilicity, and easy processability. Abundant functional surface termination groups, such as $-O$, $-OH$, and $-F$, have a crucial impact on the superior performance of the MXenes.[27,28] These surface termination groups endow MXenes with superior electronegativity, even more than polytetrafluoroethylene (PTFE).[29] MXenes are a competitive option as both negative surface and electrode owing to the excellent metallic conductivity and triboelectric negativity. Embedded into the polymer, MXenes not only endow the polymer with more electronegativity but also improve surface charge density, capacitance, charge trapping, and charge transportation via dielectric modulation and metallic conductivity.[30–33] The incorporation of MXenes, such as $Ti_3C_2T_x$ in PVDF and its copolymers, has significantly enhanced the output performance of TENGs.[20,34–37] However, all the reported works focus on the development of either film or nanofiber mat-based TENGs which lacks wearability and integration with textiles.

1D fiber-shaped devices can be processed into planar and 3D structures. These structures possess superior flexibility that allows the structure to withstand complex deformation, such as twisting, bending, folding, stretching, crack propagation, and rupture mechanics, compared to planar devices.[38,39] Moreover, the structures have the characteristic of wash-and-wear, which is necessary for long-term use, and the inherent porous structure of textiles facilitates thermal regulation. The softness of the fibers endows textile structures and enhances compatibility with the human body. These characteristics provide significant advantages to fibers for the fabrication of wearable functional devices. Conventional fiber and fabric-based TENGs are composed of complex structures and pose a significant challenge in large-scale fabrication and stability.[40] The thermal drawing process (TDP), a technology originally developed for optical fiber fabrication, has been adapted to fabricate multimaterial fibers in kilometers of length.[41,42] TDP involves the preparation of macroscopic preform with multiple components and different functionalities to be drawn into a micro-scale fiber while maintaining the structure of the preform. The preparation of preform in macro-scales provides a high degree of freedom without complex experimental setups. TDP has the capability

to draw the electrode-embedded fiber with multiple functionalities in a single step and has the potential scalability to make it suitable for industrial-scale textile manufacturing. Moreover, thermally drawn functional fibers have been used as a feed material for 3D-printed structures. The multimaterial structure is capable of preserving the inner functional structure while simultaneous phase change of the outer layer makes these fibers suitable for 3D-printed high-performance device fabrication beyond textiles.[43,44] TDP process has further enabled the continuous fabrication of semiconductor diodes and microchips embedded in single fibers.[45,46] Although this fabrication technique has guided the way for large-scale manufacturing of functional and electronics embedded fibers[45,46] for the application spanning flexible energy storage, energy generation, and sensor,[47–51] the work on nanomaterials embedded fiber is very limited due to the correlation with rheological attributes of the polymer.[52–55] Thermally drawn TENG fibers have demonstrated great promise in the scalable fabrication and compatibility with the textile weaving process.[50,56–58] Innovative approaches like embedding highly conductive liquid metal and microscale metal wire electrodes into polymer fibers, surface patterning of preforms and fibers, and utilizing stretchable elastomer fibers have enhanced the output of TENGs. However, the incorporation of high-performance 2D nanomaterials in the polymer matrix for the improvement of the functionality of thermally drawn fibers is yet to be explored.

In this study, to the best of our knowledge, we report the scalable fabrication of MXene-PVDF nanocomposite fiber by TDP for the first time. $Ti_3C_2T_x$ MXene is successfully incorporated into a thermally drawn fiber with the potential to fabricate kilometers-long fiber in a single step. We have fabricated MXene-embedded polymer fibers and evaluated the effect of MXene incorporation on the polarization of PVDF. We have demonstrated the effect of MXene concentration on the performance of TENG. The performance improves significantly due to the synergistic effect of interfacial polarization, microcapacitor formation, spontaneous β phase formation of PVDF, and increased surface roughness due to MXene incorporation. The open circuit voltage (V_{OC}) and short circuit current (I_{SC}) of 5% MXene-embedded polymer fiber experience 1.53 times and 1.58 times improvement compared to pristine PVDF polymer fiber. The flexibility allows the drawn fibers to be woven into fabric. The fabric shows a peak power (P) of 24.5 μW which corresponds to 40.8 mW m^{-2} power density (PD). We have demonstrated the energy harvesting capability of the woven fabric TENG by operating low-power electronics. Moreover, the fabric TENG shows promise as a self-powered sensor that can distinguish various human motions.

2. Results and Discussions

2.1. Fabrication of Triboelectric Fibers

The fabrication protocol of PVDF-$Ti_3C_2T_x$ MXene (PMX) nanocomposite film and the fibers are illustrated in **Figure 1**a,b. The process involves the synthesis of MXene, preparation of nanocomposite films, consolidation of films into a preform, and finally thermally drawing tens of meters of fibers from

the preform. The detailed fabrication processes are discussed in Experimental Section. Synthesis of MXene ($Ti_3C_2T_x$) started with the preparation of MAX phase (Ti_3AlC_2) precursor, followed by etching of metallic Al layer from MAX phase, and intercalation to obtain MXene.[59,60] The PMX nanocomposite films consisting of 1, 3, and 5 wt% MXene were prepared by dissolving PVDF and mixing with MXene via vigorous stirring and drying the film in an inert environment. The nanocomposite films were rolled on a conductive polyethylene (CPE) cylindrical rod, and a sacrificial layer of polycarbonate (PC) films were rolled on the nanocomposite film before the consolidation of the preform. The sacrificial layer ensures the stability of the structure during the drawing. The preform was drawn into fibers using the thermal drawing technique to produce fibers of length in the order of tens of meters with only a 15-cm-long preform (Figure S1, Supporting Information). In brief, the process involved feeding the preform into a furnace at a certain speed (v_{feed}) while maintaining a suitable temperature above the glass transition temperature (T_g) of the polymers and pulling the fibers using a capstan at a certain speed (v_{draw}). The dimension of the fibers depends on the preform shape, preform feeding speed (v_{feed}), fiber drawing velocity (v_{draw}), and drawing temperature. The final dimension of the fibers can be described[41]

$$D_{fiber} = D_{preform}\sqrt{\frac{v_{feed}}{v_{draw}}} \tag{1}$$

where D_{fiber} and $D_{preform}$ are the diameters of the fiber and the preform, respectively. Although the thermal drawing method facilitates the co-drawing of different materials, the process poses a limitation on the choice of materials. The co-drawable materials require to have similar T_g and similar complex shear viscosity (η^*) at the drawing temperature for stable fiber fabrication. Apart from the viscosity, other rheological attributes, that is, storage modulus (G'), loss modulus (G''), and the loss factor (tan δ) require careful consideration.[61] At the drawing temperature, the loss modulus or viscous component requires to dominate the storage modulus or elastic component. This criterion makes the process more complex when nanomaterials are added to the polymers as nanomaterials affect rheological properties. The incorporation of MXene significantly increases the storage modulus and complex viscosity of PVDF.[62] For this reason, MXene composition was limited by 5 wt% of PVDF in this work to ensure the successful fabrication of nanocomposite fibers. Figure 1c shows the scanning electron microscopy (SEM) images of the as-drawn fiber where the CPE core diameter is 600 µm and the thickness of the PVDF nanocomposite layer and PC sacrificial layer is 150 µm each. The etching of the PC layer leaves a functional fiber of 900 µm in diameter. The thermally drawn fibers are flexible as depicted in Figure 1d making the fibers suitable for textile processing.

2.2. Materials Characterization of Nanomaterials and Fibers

Figure 2 presents the characterization of the MAX phase and MXene to confirm the successful synthesis of MXene using SEM, X-ray diffraction (XRD), and X-ray photoelectron spectroscopy (XPS). Figure 2a,b shows SEM images of MAX phase precursor and MXene, respectively. The multilayered structure of MXene compared to the solid flat structure of the MAX phase confirms the successful etching of the Al layer. The XRD analysis as presented in Figure 2c depicts the emergence
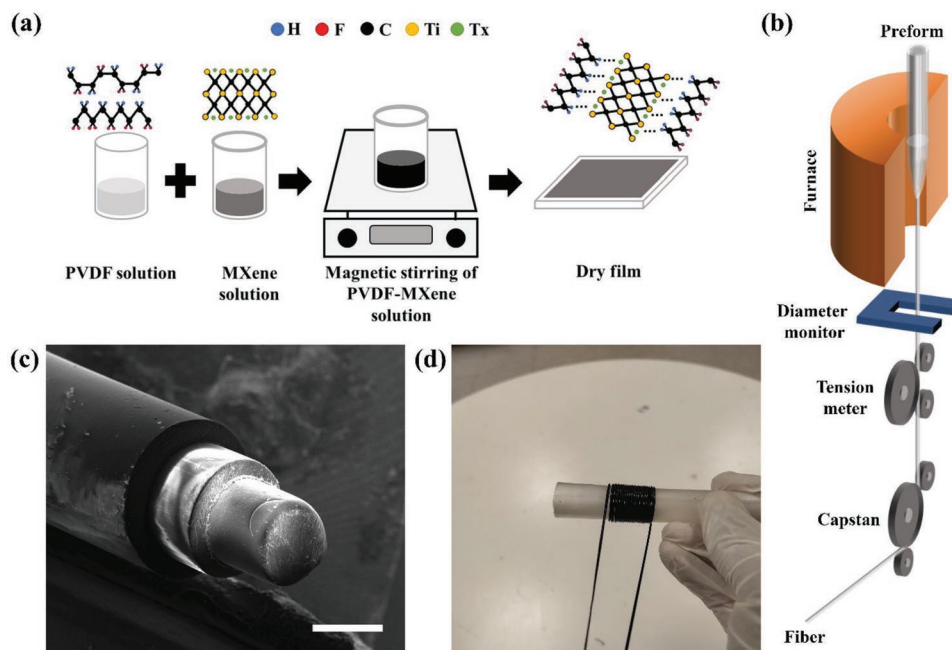

Figure 1. Fabrication process of PVDF-MXene nanocomposite fibers. Schematic of the fabrication of nanocomposite a) films and b) fibers. c) The SEM images of an as-drawn fiber. The outer layer is PC sacrificial layer, the sandwiched layer is the PVDF nanocomposite, and the center part is the CPE core. Scale bar: 500 µm. d) Flexible drawn fiber rolled on an 8 mm diameter tube.
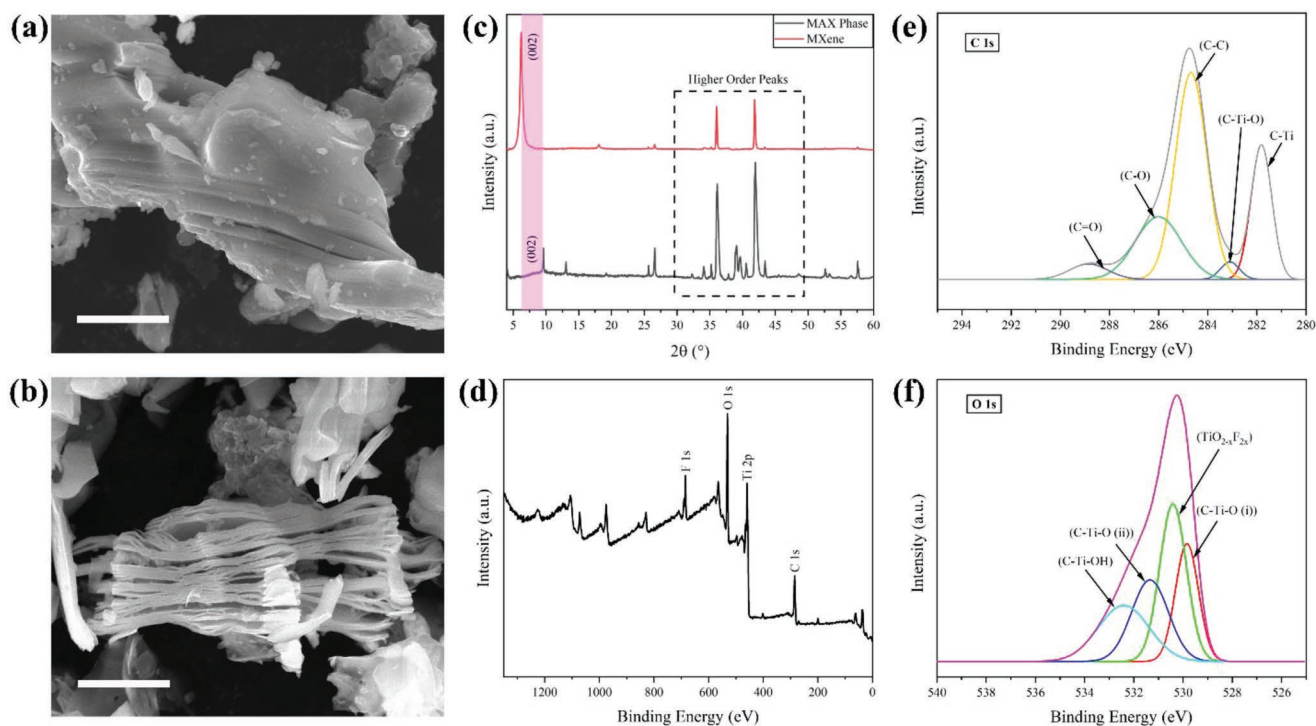
Figure 2. Characterization of synthesized MXene. SEM images of a) MAX phase and b) MXene. Scale bar: 3 μm. c) XRD spectra of MAX phase and MXene. d) XPS survey spectrum of MXene. High-resolution XPS spectrum of e) C1s and f) O1s.

of an intense (002) XRD peak at $2\theta = 6.6°$ and significant suppression of higher-order peaks supporting the proper synthesis of MXene. However, the (002) peak shifts to a lower diffraction angle compared to the MAX phase ($2\theta = 9.6°$) due to the possible intercalation of water molecules and changing d-space to 13.4 Å and c-lattice parameter to 26.8 Å.[63] The detailed XPS survey spectrum of MAX phase and MXene as shown in Figure S2a, Supporting Information, and Figure 2d shows common peaks of C1s, O1s, and Ti2p. However, the characteristic peak of Al2p at 75.72 eV disappeared, and F1s peak emerged at 685.05 eV in MXene unlike the MAX phase indicating proper etching of metallic Al layer and surface functionalization of synthesized MXene. The deconvoluted peaks of the high-resolution XPS spectrum of C1s as shown in Figure 2e at 281.9, 283.08, 284.4, 286.4, and 288.9 eV corresponds to the formation of C−Ti, C−Ti−O, C−C, C−O, and C=O bonds, respectively.[64,65] The peaks at 529.8 and 531.3 eV indicate C−Ti−O species and the 532.5 eV peak corresponds to C−Ti−OH in the high-resolution XPS spectrum of O1s in Figure 2f.[65] Moreover, the high-resolution F1s spectrum presented in Figure S2b, Supporting Information, confirms the presence of C−Ti−F and C−F at 684.6 and 686.3 eV peaks, respectively.[65,66] The detailed XPS spectrum suggests the surface functionalization of MXene with abundant oxygen-containing and F-terminated groups. The presence of such electronegative groups is necessary to enhance the performance of triboelectric materials.

The fibers were drawn from the films maintaining the same drawing condition for all the preforms, that is, PVDF fiber, PVDF-1wt% MXene (PMX-1), PVDF-3wt% MXene (PMX-3), and PVDF-5 wt% MXene (PMX-5) nanocomposite fibers.

Figure 3a shows the SEM image of the cross-section of PVDF (i) and PMX-5 (ii) nanocomposite fibers. The cross-sections of the fibers show the absence of any deformation or porosity due to the addition of MXene into the PVDF during thermal drawing suggesting excellent interfacial compatibility of MXene and PVDF polymer matrix. Figure 3b shows the surface morphology of both fibers (side view). The incorporation of MXene significantly increases the surface roughness of PMX-5 fibers compared to the PVDF fibers. Figure S3, Supporting Information, shows laser differential interference contrast (DIC) images that confirm the uniform distribution of MXene in the PMX-5 fiber over 10 m of length. Fourier transform infrared spectroscopy (FTIR) and XRD provide insight into the phase transition of PVDF polymer. PVDF polymer shows five crystalline polymorphs, that is, α, β, γ, δ, and ε phases where nonpolar α (TGTG′) and polar β (TTTT), γ (TTTGTTTG′) phases are common phases of interest.[67] The phases of the PVDF polymers depend on the thermal processing conditions.[68] FTIR spectra of PVDF film and PVDF-based fibers are presented in Figure S4a, Supporting Information, and Figure 3c, respectively. PVDF film shows characteristic peaks of α phase at 763, 795, 854, and 870 cm^{-1} with insignificant peaks of β phase at 510, 840, and 1234 cm^{-1}, and γ phase at 833 and 1279 cm^{-1}.[69] The intensity of all the exclusive peaks of α phase at 763, 795, 854, and 870 cm^{-1} peak decreases, and β phase peaks at 510, 840, and 1401 cm^{-1} increase post-thermal drawing of fibers. The intensity of characteristic β phase peaks at 510 and 840 cm^{-1} increases with MXene content in PVDF nanocomposite. The separation of β and γ phases of PVDF is difficult due to the superimposed peaks. However, the absence of any shoulder peak at 833 and 1234 cm^{-1} supports the existence of
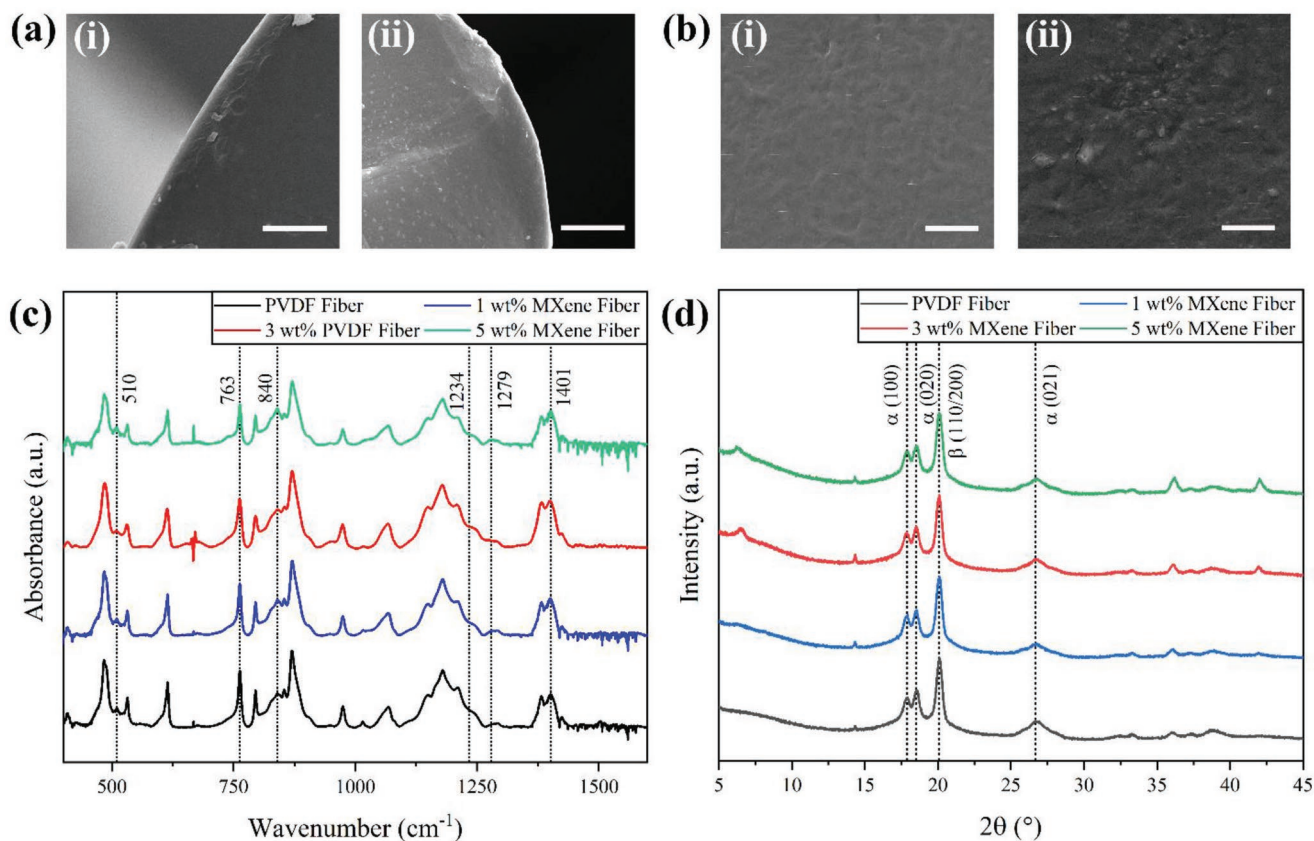
ADVANCED
SCIENCE NEWS
www.advancedsciencenews.com

NANO · MICRO
small
www.small-journal.com

Figure 3. Characterization of thermally drawn fibers. a) SEM images of the cross-section of i) PVDF fiber and ii) PMX-5 fiber. Scale bar: 20 µm. b) SEM images of the surface (side view) of i) PVDF fiber and ii) PMX-5 Fiber. Scale bar: 5 µm. c) FTIR spectra of the PVDF fiber and PVDF-MXene nanocomposite fibers with various wt%. d) XRD spectra of the PVDF fiber and PVDF-MXene nanocomposite fibers with various wt%.

the β phase. The relative fraction of β phase content, F(β) can be quantified using[70]

$$F(\beta) = \frac{A_\beta}{(K_\beta/K_\alpha)A_\alpha + A_\beta} \quad (2)$$

here, K_α and K_β values are 6.1×10^4 and 7.7×10^4 and represent the absorption coefficient at 763 and 840 cm^{-1}, respectively. A_α and A_β are the absorbance intensity at the respective wavenumber. The β phase content increases to 35% in PVDF fiber from 30% in PVDF film and the incorporation of MXene increases the β phase further up to 43% in PMX-5 fiber. Figure S4b, Supporting Information, and Figure 3d represent the XRD spectrum of PVDF film and PVDF-based fibers, respectively, to provide further information on the phase distribution of PVDF polymer. XRD spectrum of PVDF film shows peaks at diffraction angle $2\theta = 17.7°$, $18.3°$, $19.9°$, and $26.5°$ corresponding to the (100), (020), (110), and (021) planes of α phase, respectively.[71] The intensity of the peaks at 17.7°, 18.3°, and 26.5° decreases in fibers and follows a decreasing trend with the rise of MXene nanofillers content in the fibers. Furthermore, the fibers demonstrate a peak at $2\theta = 20.2°$ corresponding to the (110)/(200) plane of β phase instead of 19.9°. The minor peaks at the diffraction angle around $2\theta = 7°$ represent the (002) plane of MXene in PMX-3 and PMX-5 fiber spectra. The FTIR and XRD analysis suggests thermal drawing technique increases the relative fraction of β phase, and

MXene assists in the enhancement of β phase polarity of PVDF polymer. However, the α phase does not completely diminish in the fibers, rather α and β phases coexist in thermally drawn fibers. The improved interaction between the nanofiller and PVDF polymer chain may facilitate the nucleation of the electroactive phase and assist the formation of β crystals.[72,73] Increased β phase assists interfacial polarization utilizing the highly ordered molecular orientation compared to the other phases.[74]

2.3. Electrical Characterization of Triboelectric Fibers

Fiber TENG works based on the fundamental single-electrode mode through the coupling effect of contact electrification and electrostatic induction.[75] The output of the single electrode TENG depends on the contact-separation principle.[76] As shown in **Figure 4**a-i–v, no charge transfer between the external material-polyetherimide (PEI) and the fiber TENG (PVDF) occurs at the original state. Surface charge transfer occurs when two materials are brought in contact due to contact electrification and create a potential difference when separated. The electrostatic induction triggers electron flow from the CPE electrode to the ground and reaches equilibrium when fully separated. When the cycle continues to bring the surfaces in contact again, the electron flows from the ground to the electrode to neutralize the potential drop. The contact and separation show two characteristic
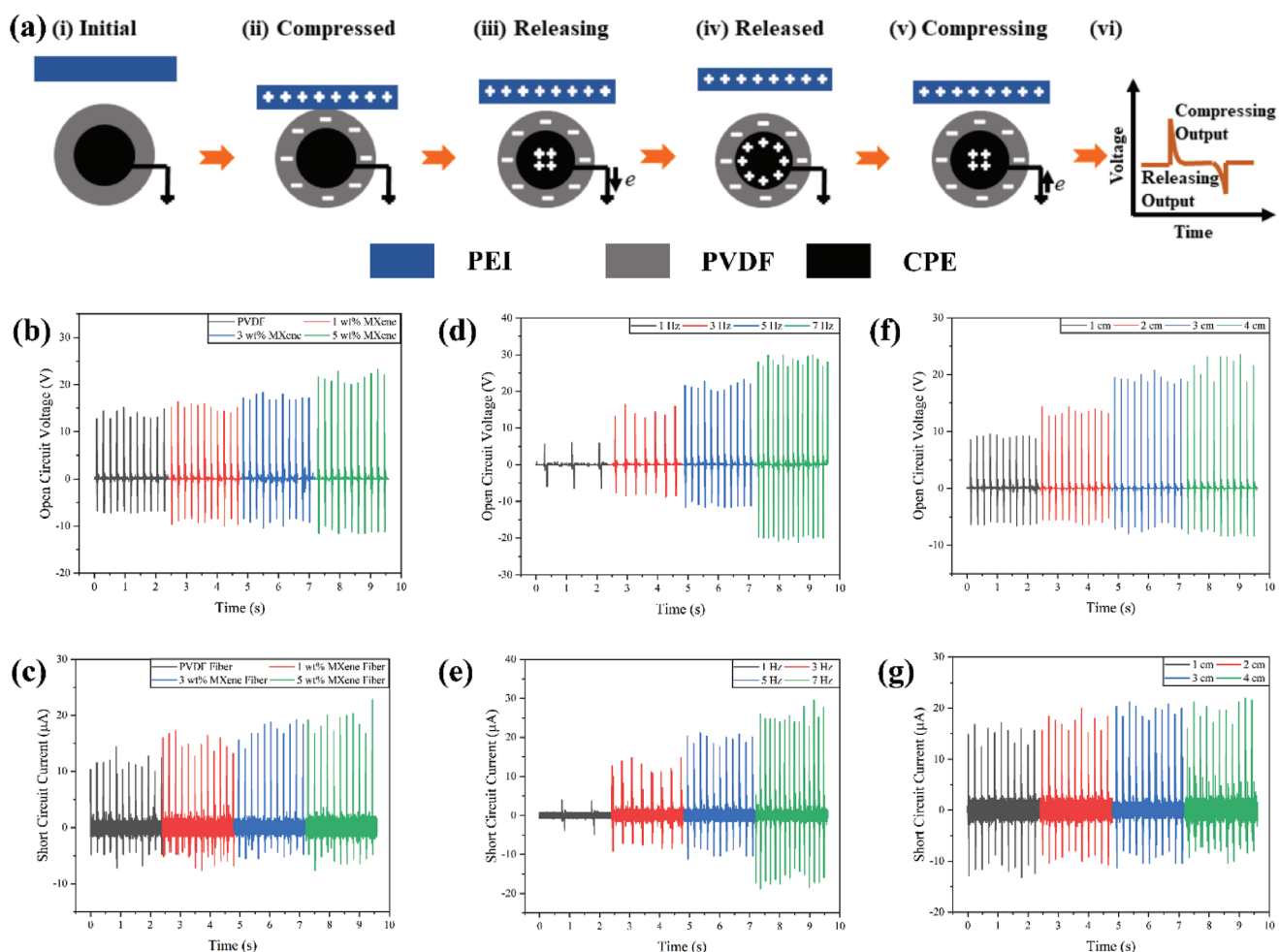
Figure 4. Electrical characterization of thermally drawn TENG fibers. a) Schematic of i–v) working principle of single electrode fiber TENG and vi) typical output for one contact-separation cycle. Waveforms of b) open circuit voltage (V_{OC}) and c) short circuit current (I_{SC}) of pristine and MXene embedded TENG fiber (contact length: 3 cm, frequency: 5 Hz). Waveforms of d) open circuit voltage (V_{OC}) and e) short circuit current (I_{SC}) of 5 wt% MXene embedded nanocomposite fibers at different frequencies (contact length: 3 cm). Waveforms of f) open circuit voltage (V_{OC}) and g) short circuit current (I_{SC}) of 5 wt% MXene embedded nanocomposite fibers at different contact lengths (frequency: 5 Hz).

peaks in opposite directions as shown in Figure 4a-vi). In this work, a custom motor ensures stable periodic contact and separation between the external surface and the TENG fiber (Figure S5, Supporting Information). A fixed stage with the PEI layer held the fiber during the characterization, and PEI was used as an external positive surface according to the triboelectric series.[77] A metal pin served as the ground as any conductor can work as the ground for single electrode mode TENG.

The output open circuit voltage (V_{OC}), short circuit charge transfer (Q_{SC}), and short circuit current (I_{SC}) of TENG in contact separation mode can be expressed by[30,78]

$$V_{OC} = \frac{\sigma S}{2C_0} \tag{3}$$

$$Q_{SC} = V_{OC} C_0 = \frac{\sigma S}{2} \tag{4}$$

$$I_{SC} = \frac{dQ}{dt} \tag{5}$$

where σ is the triboelectric charge density of the fiber surface, S is the effective contact area, C_0 is a constant representing the capacitance between the electrode and the ground, and dQ/dt is the transferred charge with time. These equations indicate the relationship between the triboelectric charge density of the surface and the output of the nanogenerator. The charge density of the surface depends on the capacitance of the functional surface and can be given as[79,80]

$$\sigma = \frac{CV}{S} = \frac{\varepsilon_0 \varepsilon_r V}{t} \tag{6}$$

$$C = \frac{\varepsilon_0 \varepsilon_r S}{t} \tag{7}$$

where C is the capacitance, ε_r is the relative permittivity, V is the surface potential of the fiber, and t is the thickness of the fiber. These equations express that the performance of the TENG can be enhanced by increasing capacitance through

**ADVANCED
SCIENCE NEWS**
www.advancedsciencenews.com

NANO · MICRO
small
www.small-journal.com

dielectric modulation of the functional surface and increasing the contact area.

Figure 4b–g shows the output waveforms of the fabricated fiber TENGs. Figure 4b,c represents the V_{OC} and I_{SC} waveforms of each TENG in terms of MXene content in the fibers. The characterization was performed for a 3 cm contact length at a 5 Hz frequency. Pristine PVDF fiber shows a peak V_{OC} of 15.2 V which increases to 23.2 V at 5% MXene addition (PMX-5 fiber), which is 1.53 times higher than the PVDF fiber. The output increases by 1.07 and 1.21 times to 16.4 and 18.4 V for PMX-1 and PMX-3 nanocomposite fibers, respectively. A similar trend follows in the case of short circuit current (I_{SC}) output. I_{SC} increases 1.58 times to reach 22.8 μA for PMX-5 nanocomposite fiber compared to the 14.4 μA for the PVDF fiber. The effect of MXene addition on the output of nanocomposite fiber TENGs can be ascribed to several factors. First, it is well reported that MXene enhances the dielectric constant of PVDF polymer which can be explained by the microscopic dipole model and the microcapatior model.[20,81] The abundant −O, −OH, and −F surface termination groups play a crucial role in the superior electronegativity of MXene and inducing interfacial polarization. The presence of polar surface termination groups facilitates interfacial interaction with the dipoles of polar polymer chains of PVDF.[82] Electrostatic interaction between the polar groups of PVDF and MXene induces polarization locking and results in the conformational transformation of PVDF from the non-polar α phase to the polar β phase.[20,83] Moreover, excellent compatibility between the PVDF matrix and MXene owing to the hydrogen bond effect facilitates numerous microcapacitor formations.[84] The intercalation of the PVDF chain between MXene nanosheets[85] and differences in dielectric permittivity between MXene and PVDF forms microcapaciotors.[86] Microcapacitors not only increase dielectric constant but also improve charge accumulation and charge storage capability.[34] The microscopic dipole and microcapacitor formation thus improve surface charge density through dielectric modulation. Second, excellent metallic conductivity and large interlayer distance of the 2D nanomaterial MXene improve the conductivity of the nanocomposite, endow the polymer with sufficient free charges and interlayer space, and improve charge transport and charge density.[87] Finally, the enhanced surface roughness due to the MXene incorporation plays role in improved output by increasing the contact surface area and triboelectric charge generation.[88] The factors synergistically improve surface charge density and thus improve the output of the MXene-embedded fibers. PMX-5 fiber response with change in frequency and contact length provides further information on fiber TENG characteristics. Figure 4d,e represents the open circuit voltage and short circuit current output of the PMX-5 fiber with a 3 cm contact length as a function of contact frequency. The fibers show a gradual increase in V_{OC} and I_{SC} output from 1 to 7 Hz. The V_{OC} reaches 6 to 30 V, and I_{SC} increases from 3.92 to 29.6 μA when the frequency is changed from 1 to 7 Hz. Short circuit current is related to charge transfer with time as shown in Equation (5) and can be attributed to the accumulated surface charges.[34] An increase in open circuit voltage despite being independent of frequency according to Equation (3) can be ascribed to the increased pressure with frequency and sur-

face charge accumulation.[89] The higher pressure leads to increased contact surface area due to the higher deformation of the fiber. Moreover, higher contact frequency prevents the natural neutralization of charges, and thus, promotes surface charge accumulation. The significant improvement in short circuit current response can be attributed to the inversely proportional relationship with time during charge transfer according to Equation (5). Figure 4f,g presents the V_{OC} and I_{SC} waveform of PMX-5 fiber with the increment of contact length at 5 Hz. V_{OC} increases from 9.6 to 23.6 V when contact length increases from 1 to 4 cm. I_{SC} also increases by 1.3 times to reach 22 from 17.2 μA upon an increment of contact length in the same manner. The increased contact length represents the increase in the effective contact area and results in an increase in capacitance. This translates into enhanced surface charge density and improved V_{OC} and I_{SC} output. V_{OC} and I_{SC} waveform generated from one contact-separation cycle is presented in Figure S6a,b, Supporting Information. Moreover, the nanocomposite fibers show stable performance even after 100 days and maintain 96% of the output (peak-to-peak open circuit voltage) as shown in Figure S7a, Supporting Information. The fiber further demonstrates excellent stability when treated in water for 24 h by preserving 94% of the output (Figure S7b, Supporting Information). The protection of MXene against oxidation is achieved by the hydrophobic nature of PVDF polymer ensuring the long-term stability of the fibers.[90] Contact angle measurement of the 5 wt% MXene embedded PVDF film confirms the hydrophobicity of the nanocomposite film as shown in Figure S8, Supporting Information. The performance evaluation of the fiber leads to the development of a textile TENG device for application in energy harvesting and the development of self-powered sensors discussed in the next section.

2.4. Triboelectric Textiles for Energy Harvesting and Self-Powered Sensing

To demonstrate the real-world application, 1 m long PMX-5 nanocomposite fiber was woven into a textile fabric with a 5 cm × 2 cm functional surface area (Figure S9, Supporting Information). **Figure 5**a–d shows the output waveforms of the fabric sensor with frequency and contact area. The V_{OC} and I_{SC} show a gradual increase in output when the frequency is increased from 1 to 7 Hz with a 6 cm^2 contact area as presented in Figure 5a,b similar to the fabricated fibers. The V_{OC} and I_{SC} response show a similar trend when tested for 2, 4, 6, and 8 cm^2 contact areas at 5 Hz of frequency as presented in Figure 5c,d. The relatively low conductivity of flexible CPE polymer electrodes hinders the significant improvement in the output response of fabric compared to the fiber. Weaving 1.2 m long fiber with low conductivity electrode increases the equivalent series resistance (ESR) of the electrode and thus limits performance enhancement during scale-up. Either connecting short-length fibers in parallel during weaving or improving the conductivity of the electrode may improve the performance.[91] However, as scalability is the major advantage of TDP, the improved output can be achieved by using a liquid metal core[57] as an electrode or convergence drawing[92] of metal wires as an electrode instead of CPE. The output response of the TENG device is AC and requires to be
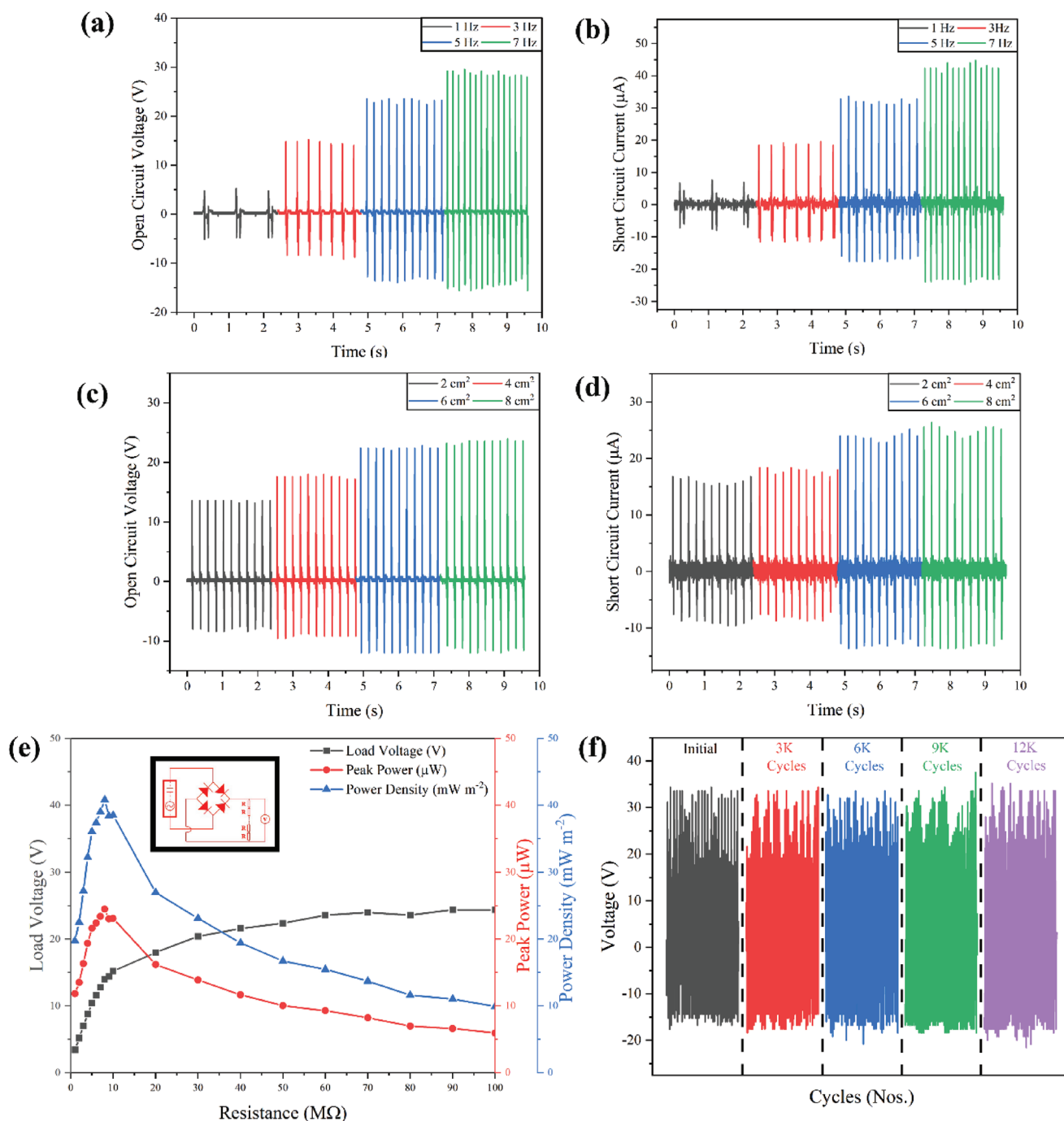
Figure 5. The electrical characterization of TENG fabrics (PMX-5). Waveforms of a) open circuit voltage (V_{OC}) (Inset: TENG fabric) and b) short circuit current (I_{SC}) of TENG fabric at different frequencies (contact area: 6 cm^2). Waveforms of c) V_{OC} and d) I_{SC} of TENG fabric at different contact areas (frequency: 5 Hz). e) Load voltage (V_L), peak power (P), and power density (PD) of TENG fabric when connected to various loads from 1 to 100 MΩ. (Inset: schematic of the electrical circuit for voltage measurement when connected to load resistors.) f) Long-term stability of TENG fabric device. The waveforms show voltage output at the beginning till 12 000 cycles of tapping at an interval of 3000 cycles.

rectified for practical use. Figure S10, Supporting Information, shows the AC open circuit voltage output of the TENG fabric and DC waveform after rectification. P and PD parameters indicate the output performance of TENG based on the external load matching and are calculated by

$$P = \frac{V_L^2}{R_L} \tag{8}$$

$$PD = \frac{P}{A} \tag{9}$$

where R_L is the load resistance. Figure 5e presents the load voltage (V_L), P, and PD of TENG fabric when connected to load resistors ranging from 1 to 100 MΩ. The V_L demonstrates a sharp increase in output when the external load is increased from 1 to 8 MΩ and gradually saturates at 24 V for higher load resistor values. The peak power reaches the highest value of 24.5 µW when connected to an 8 MΩ external load and corresponds to 40.8 mW m^{-2} power density. The output power is comparable to the recent works based on single fiber-based TENGs as presented in Table S1, Supporting Information. The internal impedance of the fabric TENG device can be calculated by considering the inherent capacitance characteristic and by fitting peak power data using[57]

$$P = \frac{V_{OC}^2 R_L}{|Z_C|^2 + R_L^2} \tag{10}$$

here, Z_C is the internal impedance of the textile fabric and V_{OC} is the open circuit voltage response. The Z_C value is calculated to be 8.16 MΩ and maximum power is expected with a matching load of 8.16 MΩ. Figure S11, Supporting Information, shows the load voltage and peak power output of PVDF fiber and PMX-5 fiber TENG. The fabric TENG shows 2.65 times increase in peak power compared to the PMX-5 fiber whereas the peak power of PMX-5 fiber increases more than 3.3 times compared to the pristine PVDF fiber TENG. The output responses connected to a load of fabric and fibers represent output for 6 cm^2 and 3 cm contact surfaces, respectively, at 5 Hz contact frequency. Figure 5f and Figure S12, Supporting Information, show the fabric output for the 12 000 compression-relaxation cycles at 5 Hz frequency. The stable V_{OC} waveform confirms the mechanical durability and reliability of the device for long-term use. Furthermore, the fabric TENG demonstrates energy harvesting capability. Hand tapping for 30 s can generate enough power to charge a 10 µF capacitor and operate a calculator and a digital clock for 4 s (Figure S13 and Video S1, Supporting Information). Running for 30 s also can generate sufficient power to operate a digital clock for 2 s. These demonstrations support the energy harvesting capability of the TENG textile fabric from biomechanical motion and lead to the evaluation of the fabric TENG as self-powered sensors.

Basic human motion, that is, finger tapping and grasping is a good way to start the performance evaluation of sensors in terms of sensitivity and selectivity. Although these terms are extensively used for the evaluation of biosensors, we find the terms adequate to describe the output response of the device for a particular action and the distinguishability of the pattern of output for different actions, respectively. Figure S14a,b, Supporting Information, shows the V_{OC} and I_{SC} waveform of the fabric swatch for finger tapping which reaches over 18 V and 25 µA output. Figure S14c,d, Supporting Information, presents the V_{OC} and I_{SC} response of 1.8 V and 0.2 µA for grasping the fabric in the hand palm. Both actions show distinguishable peaks for contact separation events (Video S2, Supporting Information). The grasping movement waveform consists of the peaks during contact separation motion, as well as the irregular friction of the fabric on the palm surface. The woven fabric shows high output even at as low force as 0.3 N for finger tapping and shows a significant increase with force as shown in Figure S15, Supporting Information.

This proves the woven fabric is capable of sensing subtle human motion with a high signal-to-noise ratio (SNR). Textile fabrics undergo various deformation during wearing such as twisting, bending, and stretching. The waveforms of the woven fabric at folded state maintains high SNR with low noise as shown in Figure S16, Supporting Information. Based on the performance of the TENG fabric for basic motion sensing, we evaluated the TENG fabric as the distributed sensor. TENG-based sensors have demonstrated potential in biomotion monitoring for healthcare applications.[93–95] The waveforms of two fabric TENG attached to the armpits (Figure S17a, Supporting Information) as shown in **Figure 6**a,b demonstrate the capability of distinguishing human activities like running and walking. The waveform of running shows higher voltage output compared to the output during walking and this trend can be attributed to the higher impact force exerted on the area of interest during running. This can be used for regular activity monitoring, as well as in sports.

To further investigate the capability of the TENG device, we have attached the two devices on the heel area of the shoe for gait analysis (Figure S17b, Supporting Information). Gait analysis is important for continuous health monitoring of Parkinson's disease and tracking disease progression. A gait cycle is characterized by four events, that is, i) heel touch, ii) toe touch, iii) heel leave, and iv) toe leave, as shown in Figure 6c. The output waveforms of the sensors are shown in Figure 6d,e. The voltage waveform in Figure 6e shows two positive peaks followed by two negative peaks corresponding to the four events to complete a gait cycle. The first smaller positive peak corresponds to heel touch followed by a positive peak with higher output upon toe touch. When both heel and toe touch the ground, the body mass is completely distributed on the feet and that is the possible reason behind the higher output of the second peak. As the sensor is integrated into the heel area, the next event of the heel leaving the ground creates an initial large separation depicted by a large negative peak. Finally, when the feet completely leave the ground, the separation cycle completes and induces a minor negative peak. This device can be used as an assistive device for rehabilitation purposes to track the walking pattern data. Thus, the fabricated TENG device has the potential as a self-powered sensor by utilizing the scavenged energy during human motion while monitoring physiological activities simultaneously.

3. Conclusion

In this study, we have demonstrated the successful fabrication of MXene-embedded PVDF fiber by the TDP. The fibers have been evaluated as TENG as a function of MXene content. The output of the fiber has increased with MXene content in the polymer matrix up to 5 wt%. The peak power of the 5 wt% MXene embedded fiber shows a 3.3 times higher output compared to pristine PVDF fiber. The fibers are drawn in tens of meters in length and can be drawn in kilometers in length using industrial-scale facilities. Moreover, the fibers are flexible enough to be compactly woven into fabrics and have the potential to be used in the industrial loom for large-scale TENG fabric production. The TENG fabric shows energy harvesting capability by operating a digital clock and calculator with simple hand-tapping motion. Moreover, the fabric demonstrates excellent performance as
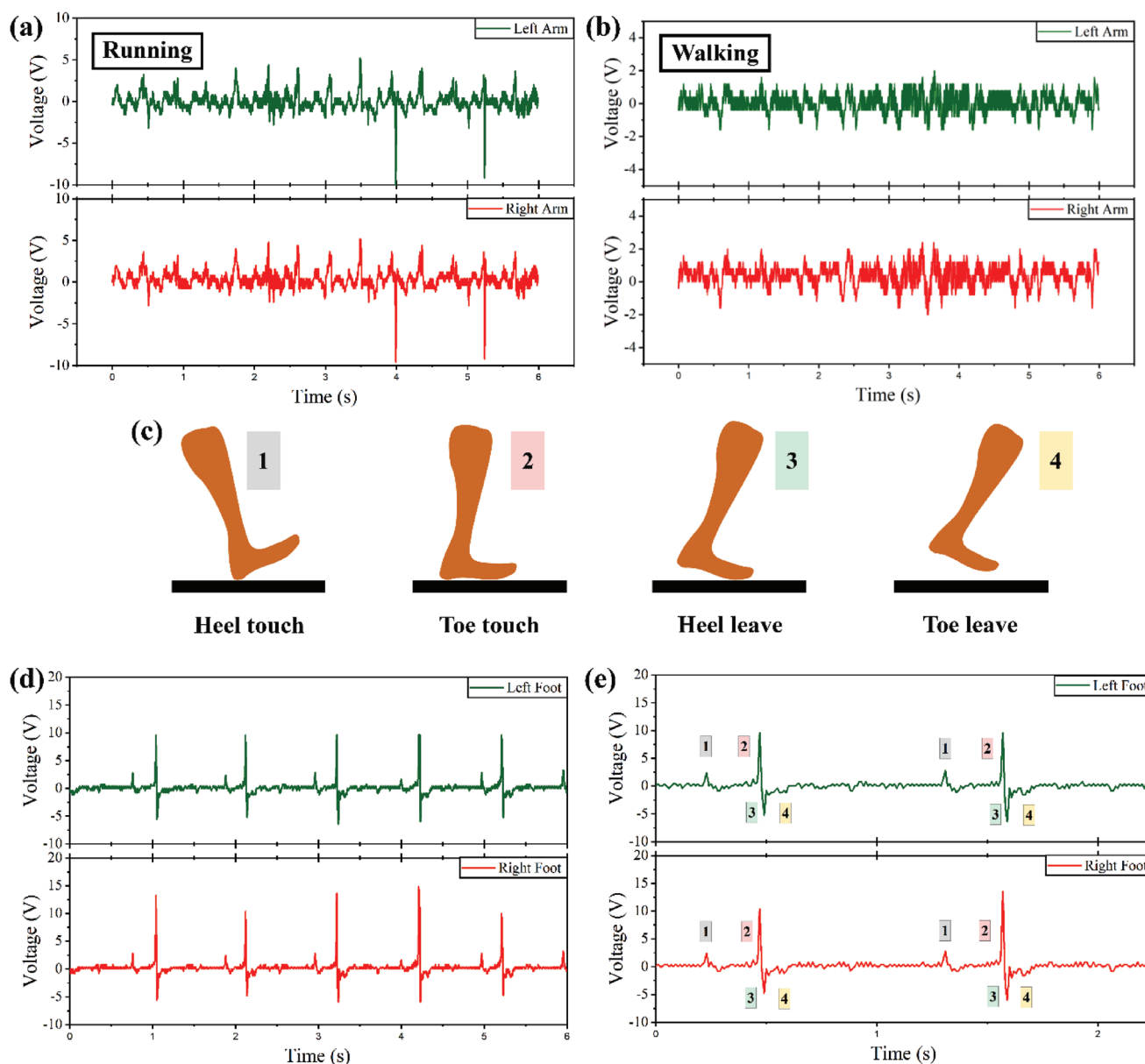
ADVANCED
SCIENCE NEWS
www.advancedsciencenews.com

NANO · MICRO
small
www.small-journal.com

Figure 6. Application of TENG fabric (PMX-5) as a self-powered sensor. Open circuit voltage waveforms of two TENG fabric devices attached to the armpits during a) running and b) walking. c) Schematic of the gait cycle. d) Open circuit voltage waveforms of two TENG fabric devices attached to the heels of the shoe sole. e) Enlarged view of the open circuit voltage waveforms of two TENG fabric devices attached to the heels of the shoe sole with indication corresponding to the events of a complete gait cycle.

a distributed sensor for human activities monitoring and gait analysis. A compact intelligent sensor module can potentially be developed by integrating a microcontroller unit for data storage and transmission with the sensor. Combined with machine learning, this sensor may function as an excellent tool for monitoring patients and tracking disease progression remotely.

4. Experimental Section

Synthesis of $Ti_3C_2T_x$ MXene: To synthesize MXene, the MAX phase was first prepared. The Ti_3AlC_2 was obtained by grinding a mixture of powders in a ball mill for 18 h. The mixture contained Ti, Al, and graphite

at molar ratios of Ti:Al:C = 3:1.1:2. To obtain a compact material, the mixed powders were cold pressed at 20 tons. The pressed material was then sintered in a tube furnace under an inert (Ar) atmosphere for 1 h at 1450 °C. Finally, the sintered compact material was pulverized in a mortar.

MXene was then obtained by wet chemical etching of Ti_3AlC_2 following previous studies with minor modifications. For the etching process, 3.35 g of NaF was mixed with 20 mL of HCl for 15 min. Then 0.5 g of Ti_3AlC_2 was added to the mixture slowly. The mixture was stirred at 60 °C for 24 h with a magnetic stirrer. The sample was then washed several times with water, 2 M hydrochloric acid, and again water. The resulting sample was centrifuged and washed with ethanol until a neutral pH value was obtained. The final MXene powder was dried in a vacuum oven at 70 °C.

The intercalation process was carried out by mixing 0.3 g of MXene powder and 10 mL of dimethyl sulfoxide at room temperature for 18 h using a magnetic stirrer. Then 6 mL of ammonia was added to this solution and stirred for 2 h. The treated samples were washed several times with water and dried in a vacuum oven at 70 °C.

Fiber Fabrication: The fiber fabrication process started with the nanocomposite film preparation. 15 wt% PVDF (Ajedium Films–Solvay Plastics) was dissolved in dimethylformamide (DMF; Carlo Erba Reagents S.A.S) at 60 °C with mechanical stirring. In the meantime, MXene was ultrasonicated in DMF solution for 1 h. After 1 h, the MXene solution was added to the PVDF solution and the process was continued for 7 more hours. After a total of 8 h, the MXene PVDF solution was poured into glass petri dishes and treated at 80 °C for 8 h to evaporate the DMF and get the PVDF-MXene nanocomposite film. CPE was the conductive electrode. CPE film was heated at 170 °C and mechanically compressed into a circular mold to prepare a cylindrical CPE rod of 10 mm. Then PVDF nanocomposite was rolled onto the CPE rod such that the diameter became 15 mm. To ensure uniform drawing, the PC (Ajedium Films) layer was rolled on top of that and the total diameter became 25 mm. Then, the preform was annealed at 90 °C in a vacuum for 24 h. The preform was consolidated later as follows: the preform was annealed at 150 °C in a vacuum for 2 h followed by consolidating at 190 °C for 45 min in a custom-built furnace. The fiber was drawn using a custom-built fiber draw tower at 240 °C and the feed speed and the drawing speed were controlled according to the desired diameter of fiber and tension during the fiber drawing. The PC sacrificial layer was dissolved using dichloromethane (DCM; Merck KGaA) to prepare the fibers for characterization.

Materials Characterization: The SEM images of the MAX phase, $Ti_3C_2T_x$ MXene, and triboelectric fibers were acquired by FEI QUANTA 200F field emission SEM. The laser DIC images were acquired using Keyence VK-X100 3D Laser Scanning Microscope. The FTIR was performed for 256 scan steps with a scan resolution of 0.5 cm^{-1} using Bruker ALPHA Platinum-ATR FTIR. The XRD analysis was performed with Pananalytical X'pert Pro XRD using Cu Kα radiation. XPS of MAX phase and MXene was performed using Thermo Fisher Scientific Kα. Contact angle measurement was performed using Dataphysics Contact Angle System OCA.

Electrical Characterization: Fibers were cut into 12 cm pieces with a 2 cm exposed CPE electrode. Conductive carbon tape was attached to the exposed electrode part to connect the fibers with the measurement device. The V_{OC} was measured using an oscilloscope and the I_{SC} was measured using the Agilent Technologies DSO1014A oscilloscope and Stanford Research Systems SR570 low noise current preamplifier. The cyclic tapping was performed using a custom-made device.

Supporting Information

Supporting Information is available from the Wiley Online Library or from the author.

Acknowledgements

Conflict of Interest

The authors declare no conflict of interest.

Author Contributions

M.H. and M.O. conceived the idea and designed the project. M.H., S.S., and I.A. contributed to fiber fabrication and electrical characterization. M.H. performed the material characterization, and formal analysis of data and prepared the original draft of the manuscript. H.P. synthesized the MAX phase and MXene. F.K.D. and M.S.O. supervised the MAX phase and MXene synthesis. M.O. supervised the project, acquired funding, and approved the manuscript. All authors contributed equally to the manuscript review and editing.

Data Availability Statement

The data that support the findings of this study are available from the corresponding author upon reasonable request.

Keywords

[1] S. Chen, J. Qi, S. Fan, Z. Qiao, J. C. Yeo, C. T. Lim, *Adv. Healthcare Mater.* **2021**, *10*, 2100116.
[2] S. D. Mamdiwar, R. Akshith, Z. Shakruwala, U. Chadha, K. Srinivasan, C.-Y. Chang, *Biosensors* **2021**, *11*, 372.
[3] P. Dwivedi, M. K. Singha, in *The Impact of the COVID-19 Pandemic on Green Societies: Environmental Sustainability* (Eds: C. Chakraborty, S. Roy, S. Sharma, T. A. Tran), Springer, New York **2021**, pp. 305–321.
[4] G. Loke, J. Alain, W. Yan, T. Khudiyev, G. Noel, R. Yuan, A. Missakian, Y. Fink, *Matter* **2020**, *2*, 786.
[5] M. Su, P. Li, X. Liu, D. Wei, J. Yang, *Nanomaterials* **2022**, *12*, 1495.
[6] J. Zhang, Y. Zhang, Y. Li, P. Wang, *Polym. Rev.* **2022**, *62*, 65.
[7] L. Avellar, G. Delgado, C. Marques, A. Frizera, A. Leal-Junior, E. Rocon, *IEEE Sens. J.* **2021**, *21*, 20078.
[8] R. Bagherzadeh, S. Abrishami, A. Shirali, A. R. Rajabzadeh, *Mater. Today Sustainability* **2022**, *20*, 100233.
[9] W. Wang, A. Yu, J. Zhai, Z. L. Wang, *Adv. Fiber Mater.* **2021**, *3*, 394.
[10] C. Zhang, W. Fan, S. Wang, Q. Wang, Y. Zhang, K. Dong, *ACS Appl. Electron. Mater.* **2021**, *3*, 2449.
[11] Z. Soleimani, S. Zoras, B. Ceranic, Y. Cui, S. Shahzad, *Nano Energy* **2021**, *89*, 106325.
[12] L. Xu, M. A. M. Hasan, H. Wu, Y. Yang, *Energies* **2021**, *14*, 6219.
[13] X. Cui, H. Wu, R. Wang, *J. Mater. Chem. A* **2022**, *10*, 15881.
[14] A. Chen, C. Zhang, G. Zhu, Z. L. Wang, *Adv. Sci.* **2020**, *7*, 2000186.
[15] J. P. Lee, J. W. Lee, J. M. Baik, *Micromachines* **2018**, *9*, 532.
[16] X. Chen, X. Han, Q.-D. Shen, *Adv. Electron. Mater.* **2017**, *3*, 1600460.
[17] X. Du, Y. Liu, J. Wang, H. Niu, Z. Yuan, S. Zhao, X. Zhang, R. Cao, Y. Yin, N. Li, C. Zhang, Y. Xing, W. Xu, C. Li, *ACS Appl. Mater. Interfaces* **2018**, *10*, 25683.
[18] H. H. Singh, N. Khare, *Energy* **2019**, *178*, 765.
[19] Y. Song, J. Bao, Y. Hu, H. Cai, C. Xiong, Q. Yang, H. Tian, Z. Shi, *Sustainable Energy Fuels* **2022**, *6*, 2377.
[20] Z. Song, W. Li, H. Kong, Y. Bao, N. Wang, W. Wang, Y. Ma, Y. He, S. Gan, L. Niu, *Nano Energy* **2022**, *92*, 106759.
[21] H. Jiang, H. Lei, Z. Wen, J. Shi, D. Bao, C. Chen, J. Jiang, Q. Guan, X. Sun, S.-T. Lee, *Nano Energy* **2020**, *75*, 105011.

[22] B. V. Tawade, I. E. Apata, M. Singh, P. Das, N. Pradhan, A. M. Al-Enizi, A. Karim, D. Raghavan, *Nanotechnology* **2021**, *32*, 142004.

[23] J. Hu, S. Zhang, B. Tang, *Energy Storage Mater.* **2021**, *37*, 530.

[24] V. Kumar, P. Kumar, R. Deka, Z. Abbas, S. M. Mobin, *Chem. Rec.* **2022**, *22*, e202200067.

[25] M. Javadi, A. Heidari, S. Darbari, *Curr. Appl. Phys.* **2018**, *18*, 361.

[26] F. F. Hatta, M. A. S. M. Haniff, M. A. Mohamed, *Int. J. Energy Res.* **2022**, *46*, 544.

[27] M. M. Hasan, M. M. Hossain, H. K. Chowdhury, *J. Mater. Chem. A* **2021**, *9*, 3231.

[28] S. T. Mahmud, M. M. Hasan, S. Bain, S. T. Rahman, M. Rhaman, M. M. Hossain, M. Ordu, *ACS Mater. Lett.* **2022**, *4*, 1174.

[29] Y. Dong, S. S. K. Mallineni, K. Maleski, H. Behlow, V. N. Mochalin, A. M. Rao, Y. Gogotsi, R. Podila, *Nano Energy* **2018**, *44*, 103.

[30] M. T. Rahman, S. M. S. Rana, M. Salauddin, M. A. Zahed, S. Lee, E.-S. Yoon, J. Y. Park, *Nano Energy* **2022**, *100*, 107454.

[31] X. Chen, Y. Liu, Y. Sun, T. Zhao, C. Zhao, T. A. Khattab, E. G. Lim, X. Sun, Z. Wen, *Nano Energy* **2022**, *98*, 107236.

[32] X. Chen, Y. Zhao, F. Wang, D. Tong, L. Gao, D. Li, L. Wu, X. Mu, Y. Yang, *Adv. Sci.* **2022**, *9*, 2103957.

[33] C. Ma, M.-G. Ma, C. Si, X.-X. Ji, P. Wan, *Adv. Funct. Mater.* **2021**, *31*, 2009524.

[34] S. M. S. Rana, M. T. Rahman, M. Salauddin, S. Sharma, P. Maharjan, T. Bhatta, H. Cho, C. Park, J. Y. Park, *ACS Appl. Mater. Interfaces* **2021**, *13*, 4955.

[35] T. Bhatta, P. Maharjan, H. Cho, C. Park, S. H. Yoon, S. Sharma, M. Salauddin, M. T. Rahman, S. S. Rana, J. Y. Park, *Nano Energy* **2021**, *81*, 105670.

[36] H. Xu, J. Tao, Y. Liu, Y. Mo, R. Bao, C. Pan, *Small* **2022**, *18*, 2202477.

[37] C. Jiang, C. Wu, X. Li, Y. Yao, L. Lan, F. Zhao, Z. Ye, Y. Ying, J. Ping, *Nano Energy* **2019**, *59*, 268.

[38] X. Xu, S. Xie, Y. Zhang, H. Peng, *Angew. Chem., Int. Ed.* **2019**, *58*, 13643.

[39] W. Zeng, L. Shu, Q. Li, S. Chen, F. Wang, X.-M. Tao, *Adv. Mater.* **2014**, *26*, 5310.

[40] K. Dong, X. Peng, Z. L. Wang, *Adv. Mater.* **2020**, *32*, 1902549.

[41] G. Loke, W. Yan, T. Khudiyev, G. Noel, Y. Fink, *Adv. Mater.* **2020**, *32*, 1904911.

[42] W. Yan, C. Dong, Y. Xiang, S. Jiang, A. Leber, G. Loke, W. Xu, C. Hou, S. Zhou, M. Chen, R. Hu, P. P. Shum, L. Wei, X. Jia, F. Sorin, X. Tao, G. Tao, *Mater. Today* **2020**, *35*, 168.

[43] L. van der Elst, C. F. de Lima, M. G. Kurtoglu, V. N. Koraganji, M. Zheng, A. Gumennik, *Adv. Fiber Mater.* **2021**, *3*, 59.

[44] G. Loke, R. Yuan, M. Rein, T. Khudiyev, J. Jain, J. Joannopoulos, Y. Fink, *Nat. Commun.* **2019**, *10*, 4010.

[45] M. Rein, V. D. Favrod, C. Hou, T. Khudiyev, A. Stolyarov, J. Cox, C.-C. Chung, C. Chhav, M. Ellis, J. Joannopoulos, Y. Fink, *Nature* **2018**, *560*, 214.

[46] G. Loke, T. Khudiyev, B. Wang, S. Fu, S. Payra, Y. Shaoul, J. Fung, I. Chatziveroglou, P.-W. Chou, I. Chinn, W. Yan, A. Gitelson-Kahn, J. Joannopoulos, Y. Fink, *Nat. Commun.* **2021**, *12*, 3317.

[47] T. Khudiyev, J. T. Lee, J. R. Cox, E. Argentieri, G. Loke, R. Yuan, G. H. Noel, R. Tatara, Y. Yu, F. Logan, J. Joannopoulos, Y. Shao-Horn, Y. Fink, *Adv. Mater.* **2020**, *32*, 2004971.

[48] T. Khudiyev, B. Grena, G. Loke, C. Hou, H. Jang, J. Lee, G. H. Noel, J. Alain, J. Joannopoulos, K. Xu, J. Li, Y. Fink, J. T. Lee, *Mater. Today* **2022**, *52*, 80.

[49] A. Leber, C. Dong, R. Chandran, T. D. Gupta, N. Bartolomei, F. Sorin, *Nat. Electron.* **2020**, *3*, 316.

[50] M. Chen, Z. Wang, Q. Zhang, Z. Wang, W. Liu, M. Chen, L. Wei, *Nat. Commun.* **2021**, *12*, 1416.

[51] T. Zhang, K. Li, J. Zhang, M. Chen, Z. Wang, S. Ma, N. Zhang, L. Wei, *Nano Energy* **2017**, *41*, 35.

[52] X. Lu, H. Qu, M. Skorobogatiy, *ACS Nano* **2017**, *11*, 2103.

[53] W. Yan, G. Noel, G. Loke, E. Meiklejohn, T. Khudiyev, J. Marion, G. Rui, J. Lin, J. Cherston, A. Sahasrabudhe, J. Wilbert, I. Wicaksono, R. W. Hoyt, A. Missakian, L. Zhu, C. Ma, J. Joannopoulos, Y. Fink, *Nature* **2022**, *603*, 616.

[54] Y. Guo, S. Jiang, B. J. B. Grena, I. F. Kimbrough, E. G. Thompson, Y. Fink, H. Sontheimer, T. Yoshinobu, X. Jia, *ACS Nano* **2017**, *11*, 6574.

[55] Y. Zhang, X. Li, J. Kim, Y. Tong, E. G. Thompson, S. Jiang, Z. Feng, L. Yu, J. Wang, D. S. Ha, H. Sontheimer, B. N. Johnson, X. Jia, *Adv. Opt. Mater.* **2021**, *9*, 2001815.

[56] Z. Feng, S. Yang, S. Jia, Y. Zhang, S. Jiang, L. Yu, R. Li, G. Song, A. Wang, T. Martin, L. Zuo, X. Jia, *Nano Energy* **2020**, *74*, 104805.

[57] C. Dong, A. Leber, T. D. Gupta, R. Chandran, M. Volpi, Y. Qu, T. Nguyen-Dang, N. Bartolomei, W. Yan, F. Sorin, *Nat. Commun.* **2020**, *11*, 3537.

[58] Z. Wang, T. Wu, Z. Wang, T. Zhang, M. Chen, J. Zhang, L. Liu, M. Qi, Q. Zhang, J. Yang, W. Liu, H. Chen, Y. Luo, L. Wei, *Nat. Commun.* **2020**, *11*, 3842.

[59] J. Zhang, S. Li, H. Hu, Y. Zhou, *Materials* **2018**, *11*, 1979.

[60] F. Liu, A. Zhou, J. Chen, J. Jia, W. Zhou, L. Wang, Q. Hu, *Appl. Surf. Sci.* **2017**, *416*, 781.

[61] Y. Qu, T. Nguyen-Dang, A. G. Page, W. Yan, T. D. Gupta, G. M. Rotaru, R. M. Rossi, V. D. Favrod, N. Bartolomei, F. Sorin, *Adv. Mater.* **2018**, *30*, 1707251.

[62] W. Wu, W. Zhao, Q. Sun, B. Yu, X. Yin, X. Cao, Y. Feng, R. K. Y. Li, J. Qu, *Compos. Commun.* **2021**, *23*, 100562.

[63] M. Shekhirev, C. E. Shuck, A. Sarycheva, Y. Gogotsi, *Prog. Mater. Sci.* **2021**, *120*, 100757.

[64] W. Li, Z. Song, J. Zhong, J. Qian, Z. Tan, X. Wu, H. Chu, W. Nie, X. Ran, *J. Mater. Chem. C* **2019**, *7*, 10371.

[65] V. Natu, M. Benchakar, C. Canaff, A. Habrioux, S. Célérier, M. W. Barsoum, *Matter* **2021**, *4*, 1224.

[66] M. Benchakar, L. Loupias, C. Garnero, T. Bilyk, C. Morais, C. Canaff, N. Guignard, S. Morisset, H. Pazniak, S. Hurand, P. Chartier, J. Pacaud, V. Mauchamp, M. W. Barsoum, A. Habrioux, S. Célérier, *Appl. Surf. Sci.* **2020**, *530*, 147209.

[67] Z. Yin, B. Tian, Q. Zhu, C. Duan, *Polymers* **2019**, *11*, 2033.

[68] V. Tiwari, G. Srivastava, *J. Polym. Res.* **2014**, *21*, 587.

[69] X. Cai, T. Lei, D. Sun, L. Lin, *RSC Adv.* **2017**, *7*, 15382.

[70] R. Gregorio Jr., M. Cestari, *J. Polym. Sci., Part B: Polym. Phys.* **1994**, *32*, 859.

[71] P. Martins, A. C. Lopes, S. Lanceros-Mendez, *Prog. Polym. Sci.* **2014**, *39*, 683.

[72] N. Maity, A. Mandal, A. K. Nandi, *Polymer* **2016**, *103*, 83.

[73] S. Ippili, V. Jella, A. M. Thomas, C. Yoon, J.-S. Jung, S.-G. Yoon, *J. Mater. Chem. A* **2021**, *9*, 15993.

[74] K. Rajavel, S. Luo, Y. Wan, X. Yu, Y. Hu, P. Zhu, R. Sun, C. Wong, *Composites, Part A* **2020**, *129*, 105693.

[75] J. Luo, Z. L. Wang, *EcoMat* **2020**, *2*, e12059.

[76] G. Zhu, B. Peng, J. Chen, Q. Jing, Z. L. Wang, *Nano Energy* **2015**, *14*, 126.

[77] M. Kanik, M. G. Say, B. Daglar, A. F. Yavuz, M. H. Dolas, M. M. El-Ashry, M. Bayindir, *Adv. Mater.* **2015**, *27*, 2367.

[78] S. M. S. Rana, M. A. Zahed, M. T. Rahman, M. Salauddin, S. H. Lee, C. Park, P. Maharjan, T. Bhatta, K. Shrestha, J. Y. Park, *Adv. Funct. Mater.* **2021**, *31*, 2105110.

[79] K. Shrestha, S. Sharma, G. B. Pradhan, T. Bhatta, P. Maharjan, S. S. Rana, S. Lee, S. Seonu, Y. Shin, J. Y. Park, *Adv. Funct. Mater.* **2022**, *32*, 2113005.

[80] V. Harnchana, H. V. Ngoc, W. He, A. Rasheed, H. Park, V. Amornkitbamrung, D. J. Kang, *ACS Appl. Mater. Interfaces* **2018**, *10*, 25263.

[81] S. Tu, Q. Jiang, X. Zhang, H. N. Alshareef, *ACS Nano* **2018**, *12*, 3369.

[82] S. Wang, H.-Q. Shao, Y. Liu, C.-Y. Tang, X. Zhao, K. Ke, R.-Y. Bao, M.-B. Yang, W. Yang, *Compos. Sci. Technol.* **2021**, *202*, 108600.

[83] N. A. Shepelin, P. C. Sherrell, E. N. Skountzos, E. Goudeli, J. Zhang, V. C. Lussini, B. Imtiaz, K. A. S. Usman, G. W. Dicinoski, J. G. Shapter, J. M. Razal, A. V. Ellis, *Nat. Commun.* **2021**, *12*, 3171.

[84] Y. Feng, Q. Deng, C. Peng, J. Hu, Y. Li, Q. Wu, Z. Xu, *J. Mater. Chem. C* **2018**, *6*, 13283.

[85] S. Jang, H. Kim, Y. Kim, B. J. Kang, J. H. Oh, *Appl. Phys. Lett.* **2016**, *108*, 143901.

[86] Y.-W. Cai, X.-N. Zhang, G.-G. Wang, G.-Z. Li, D.-Q. Zhao, N. Sun, F. Li, H.-Y. Zhang, J.-C. Han, Y. Yang, *Nano Energy* **2021**, *81*, 105663.

[87] Y. Tian, Y. An, B. Xu, *Nano Energy* **2022**, *101*, 107556.

[88] S. Sriphan, N. Vittayakorn, *Smart Mater. Struct.* **2018**, *27*, 105026.

[89] N. Gogurla, B. Roy, J.-Y. Park, S. Kim, *Nano Energy* **2019**, *62*, 674.

[90] L. Li, X. Fu, S. Chen, S. Uzun, A. S. Levitt, C. E. Shuck, W. Han, Y. Gogotsi, *ACS Appl. Mater. Interfaces* **2020**, *12*, 15362.

[91] T. Jing, B. Xu, J. H. Xin, X. Guan, Y. Yang, *J. Mater. Chem. A* **2021**, *9*, 12331.

[92] J. S. Marion, N. Gupta, H. Cheung, K. Monir, P. Anikeeva, Y. Fink, *Adv. Mater.* **2022**, *34*, 2201081.

[93] L. Wang, H. Xu, F. Huang, X. Tao, Y. Ouyang, Y. Zhou, X. Mo, *Nanomaterials* **2022**, *12*, 3217.

[94] X. Guo, T. He, Z. Zhang, A. Luo, F. Wang, E. J. Ng, Y. Zhu, H. Liu, C. Lee, *ACS Nano* **2021**, *15*, 19054.

[95] J. Yu, X. Hou, M. Cui, S. Zhang, J. He, W. Geng, J. Mu, X. Chou, *Nano Energy* **2019**, *64*, 103923.